Mathematical Modelling on Chemically Reacting Boundary Type Flow under Reduced Gravity Conditions

Hui Ying WANG[1] **and Thomas HERVIOU**
Institut Pprime (C.N.R.S.-U.P.R. 3346)
Département Fluide-Thermique-Combustion
ENSMA - BP 40109
Téléport 2, 1 av Clément ADER
F-86961 FUTUROSCOPE CHASSENEUIL Cedex
FRANCE

E-mail: wang@ensma.fr

Abstract. A numerical study was performed to give a quantitative description of a heavily sooting, non-premixed laminar flame established in a shear boundary layer in microgravity. The competition between fuel pyrolysis rate, radiation loss due to soot formation and oxygen-side diffusion creates a number of unusual phenomena. A three-dimensional, laminar diffusion flame over plate in low-speed concurrent flow was formulated and solved. The model consists of full Navier-Stokes equations for mass, momentum, energy and species. Gas radiation associated with soot formation is included. The PAH inception model, which is based on the formation of two and three-ringed aromatic species, reproduces correctly the measured soot from a laminar ethylene diffusion flame. The flame standoff distance is beyond the boundary layer thickness, while soot resides always within the boundary layer. The fraction of the total energy released by the flame to the surface increases with a rise of pyrolysis rate due to increase in the flame volume. The zone of the high heat flux increases noticeably when the flame becomes most obviously dual on the cross-stream section due to development of the counter-rotating vortex.

1. Introduction

A fire on board spacecraft is, though unlikely owe to strict safety measures, one of the scenarios with the highest damage potential for hardware and crew. In spacecraft, where buoyancy is negligible, the flow is limited to that induced by the ventilation system with a characteristic velocity of 0.2 m/s. The most likely scenario of a flame incidentally initiated and spread on board of a spacecraft is a wall of combustible material adjacent to a low Reynolds number gas flow and exposed to a potential ignition source. When analysing a combustion process, transport equations can be scaled and characteristic parameters can be extracted. In normal-gravity, a buoyantly induced velocity generates an upper limit for all time scales and dominates all forms of transport. All forms of transport slower than natural convection can thus be neglected. In micro-gravity, this upper limit disappears and different phenomena, negligible in normal gravity, become relevant and sometimes of great importance. All characteristic time scales increase, the natures of heat/mass transfers, species (i.e. fuel and soot) generation, degradation of material change. Ignition includes solid and gas phase processes. Proper selection of materials to minimize the potential of a fire is labelled material flammability. The

processes related to the gas phase are solely affected by buoyancy and thus require particular attention. The gas phase induction period can be reduced to negligible time by introducing a pilot.

Under microgravity conditions, as a major portion of heat released from the igniting stage of combustion is transported by forced convection in the flow direction, the superior mode of spread is of co-current (forward) type. Such flame propagation in a microgravity environment is of scientific interest and also essential for the improvement of fire safety in spacecraft and space station. The work of Olson et al. [1] showed that for a forward diffusion flame, radiation becomes the predominant mode of heat transfer. Pyrolysis kinetics have an important role on the onset temperature for pyrolysis of condensed fuel but rapidly fuel generation is limited by transport of oxygen to the surface and of fuel from the interior of the material [2]. A proper evaluation of material flammability requires a detailed understanding of the effect of pyrolysis rate on soot formation, to which the structure of the flame connects [2]. Konsur et al. [3] have attempted to describe the sooting behaviour of non-buoyant jet diffusion flame by using the Smoke-Point concept proposed originally by Markstein et al. [4]. Co-current flame spread over a solid plate could then be linked to a critical soot concentration [2] controlling the trailing edge quenching. Several experimental investigations [5, 6] have demonstrated how changes in blowing affect soot formation and thus, flame structure in the absence of natural convection. Numerical simulations have been performed [7] to determine two regimes (attached and detached flows) of a low Reynolds number flow in the absence of natural convection, function of blowing and thermal expansion, but without radiation.

This is because the ratio of flame length to flame width is usually greater than unity, which implies that the flame is three-dimensional in nature. Many flame spread studies in microgravity were intended to observe the flame behaviour in a two-dimensional (2D) configuration [5, 6]. Besides, by necessity, the experiments were generally conducted in spatially limited experimental volumes which resulted in relatively narrow samples (3-5 cm) despite the original intention of a 2D experimental configuration [5, 6]. It is, therefore, critically important to determine the three-dimensional (3D) effects on flame behaviour and radiation flux as a function of pyrolysis rate, as in this paper. Currently, for predicting soot concentration, extensive efforts are devoted in 3D CFD codes to the semi-empirical soot models [8-12], involving the inception, coagulation, surface growth and oxidation processes. Non-buoyant ethylene laminar jet diffusion flames have been modelled by assuming the nucleation and growth of soot are first-order functions of acetylene concentrations [8, 9]. Recent research suggests that the growth of aromatics is the rate limiting step rather than the formation of the first ring [10]. Vovelle et al. [11] showed that in decane flames, aromatic hydrocarbons are formed from acetylene. Anderson et al. [12] have shown that even a small quantity of aromatic hydrocarbons in the fuel can significantly increase soot emissions. In the present work, the soot model, developed by Hall et al. [13], is applied to a boundary type laminar flame under microgravity. In such soot model, the soot inception rate is based on the formation of two and three-ringed aromatic species from single ring aromatic species from a detailed kinetic reaction mechanism [14].

2. Theoretical analysis

The strong coupling between soot and radiation are studied in three-dimensional flames by solving the Navier-Stokes fluid dynamic equations of elliptic, reacting flow. Binary diffusion coefficients, thermal conductivity and viscosity coefficients are all temperature and composition dependent. This set consists of the conservation equations of mass, momentum, energy and species. The precise formulation of the differential equations describing the dynamic model and the numerical technique can be found elsewhere [15], and will not be repeated here.

2.1. Combustion model

For providing the local concentration of soot precursory species, such as acetylene (C_2H_2), benzene (C_6H_6) and phenyl (C_6H_5), a detailed kinetic reaction [14], including 736 reversible reactions and 99

species has to be used to model the combustion for ethylene/air. This reaction mechanism consists of a set of elementary reactions with corresponding rate parameters. The rate coefficient for reaction is calculated from an Arrhenius expression. These rate parameters, together with the elementary reactions and their stoichiometric coefficients, constitute the reaction mechanism. The rate laws for the species can be calculated by using a time consuming stiff ODE solvers. However, any attempt to use Arrhenius expression for a detailed kinetic [14] coupled with a three dimensional elliptic, reacting flow is discouraged due to a problem of computational cost.

In combustion, the mixture fraction is a conserved quantity traditionally defined as the (mass) fraction of the gas mixture that originates in the fuel stream. The mixture fraction is a function of space and time, commonly denoted $Z(x_i, t)$. Therefore, many combustion models employ a detailed, cost effective kinetic reaction by tabulating the kinetics in terms of mixture fraction and only the mixture fraction is tracked in the calculation [16]. This implies that all species of interest of combustion products can be described in terms of the mixture fraction alone. The correspondence between the mass fraction of an individual species and the mixture fraction is called its "state relation". This state relation can be obtained by using the OPPDIF (Opposed Diffusion Flames) computer code [17] which is performed by using subroutines from the chemical program library Chemkin.

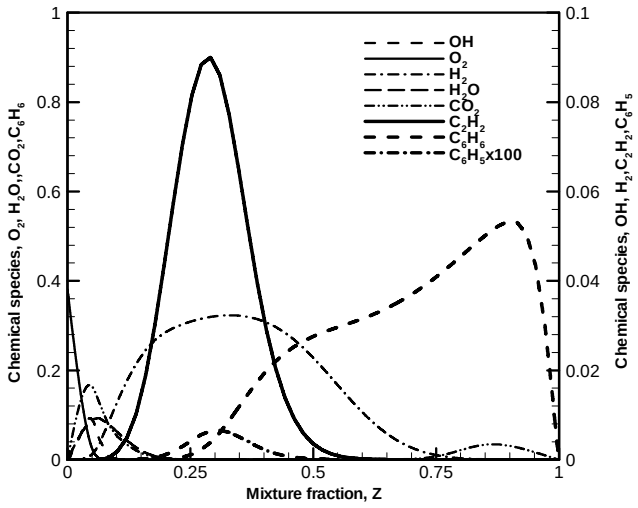

Figure 1. State relation between chemical species and mixture fraction

For obtaining such state relation for combustion of fuel/air, OPPDIF [17] requires the chemical and physical input parameters, such as the fuel type, the initial temperature values of fuel and oxygen, the initial values of fuel and oxygen mass fraction, pressure and strain rate. While this state relation is independent of reactant and oxidizer flow rates. A small value of the strain rate (<0.0003) which is much lower than the critical extinction value, is assigned, corresponding to the chemical equilibrium conditions. At the start of a simulation, the detailed chemical species involved are tabulated as a function of mixture fraction, as shown in figure 1. During the simulation, the local value of all the species is found by table-lookup according to the local mixture fraction value.

Based on the assumption that combustion is mixing-controlled, a linear combination of the conservation equation for fuel and oxidizer leads to the following transport equation for the mixture fraction, Z, a conserved quantity from a normalized mass ratio between fuel and oxidizer.

$$\frac{\partial \rho Z}{\partial t} + \frac{\partial (\rho u_i Z)}{\partial x_j} - \frac{\partial}{\partial x_j}\left(\frac{\mu}{Sc}\frac{\partial Z}{\partial x_j}\right) = 0 \qquad (1)$$

The oxygen mass conservation equation is given as,

$$\frac{\partial \rho Y_o}{\partial t}+\frac{\partial(\rho u_i Y_o)}{\partial x_j}-\frac{\partial}{\partial x_j}\left(\frac{\mu}{Sc}\frac{\partial Yo}{\partial x_j}\right)=-\frac{dY_O}{dZ}\bigg|_{Z<Z_{st}}\frac{\mu}{Sc}\nabla Z\cdot\vec{n} \quad (2)$$

where x_j represents the co-ordinate system, and μ denotes the dynamic viscosity, Sc Schmidt number equal to 0.7. For simulation of a laminar diffusion flame, the grid resolution should be sufficient fine (about 1 mm near the reaction zone) to resolve the flame sheet. The heat release rate is directly proportional to the oxygen consumption rate [15] derived from the source term of Eq.(2) at grid cell as a function of the mixture fraction, Z.

2.2. Radiative heat transfer

For a heavily sooting flame such as fire, radiation is a crucial aspect of combustion, and can dominate other modes of heat transfer. A radiative transfer equation (RTE) is solved by using a discrete expression adapted to a finite volume method [15].

$$\vec{\nabla}.\vec{\Omega}I+\kappa I=\kappa\frac{\sigma T^4}{\pi} \quad (3)$$

For simplicity, six bands are selected to give an accurate representation of the most important radiation bands of CO_2 and H_2O (RadCal) [18]. The effect of soot concentration on radiation is included by adding the radiation coefficient of soot κ_s, into that of gas κ_g. As the radiation spectrum of soot is continuous, it is assumed that the mixture of soot and gas behaves as a gray medium with a mean absorption coefficient, $\kappa=\kappa_s+\kappa_g$. The soot absorption coefficient is calculated as a function of the temperature, T, and soot mass density, M :

$$\kappa_s=1225TM/\rho_{soot} \quad (4)$$

2.3. Soot formation model

The two time-dependent conservation equations for soot particles number, N (particles/m^3) and soot mass density, M (kg/m^3) are incorporated in FDS [15].

$$\frac{\partial \rho N}{\partial t}+\frac{\partial\left[\rho N(u_i+u_i^{th})\right]}{\partial x_j}-\frac{\partial}{\partial x_j}\left(\frac{\mu}{Sc}\frac{\partial N}{\partial x_j}\right)=\dot{\omega}_{N,inc}+\dot{\omega}_{N,coa} \quad (5)$$

$$\frac{\partial \rho M}{\partial t}+\frac{\partial\left[\rho M(u_i+u_i^{th})\right]}{\partial x_j}-\frac{\partial}{\partial x_j}\left(\frac{\mu}{Sc}\frac{\partial M}{\partial x_j}\right)=\dot{\omega}_{M,inc}+\dot{\omega}_{M,gro}+\dot{\omega}_{M,oxi} \quad (6)$$

where u_i^{th} is the thermophoretic velocity components :

$$u_i^{th}=-0.54\frac{\mu}{\rho}\frac{\partial \ln T}{\partial x_i} \quad (7)$$

Several theoretical and experimental works [10, 11, 13], highlight the importance of poly-aromatics species (PAH) as result of intermediary reactions in soot inception processes. Hall et al. [13] developed a soot inception model, which is based on the formation rates of two and three ringed aromatics ($C_{10}H_7$ and $C_{14}H_{10}$) from acetylene (C_2H_2), benzene (C_6H_6) and the phenyl radical (C_6H_5). The growth mechanism of PAH is composed of consecutive repeated reactions that can be

classified in two steps mechanism, called HACA (H-Abstraction-C_2H_2-Addition). The first one is an abstraction mechanism of hydrogen.

$$2C_2H_2 + C_6H_5 \rightarrow C_{10}H_7 + H_2 \quad (8)$$

The second one is the addition reaction of acetylene.

$$C_2H_2 + C_6H_6 + C_6H_5 \rightarrow C_{14}H_{10} + H_2 + H \quad (9)$$

The first term in Eq.(5) represents the rate of soot particle inception, and the resulting expression is as,

$$\dot{\omega}_{N,inc} = \frac{8N_A}{M_p}\left\{c_2\left[\left(\frac{\rho Y_{C_2H_2}}{W_{C_2H_2}}\right)^2 \frac{Y_{C_6H_6} W_{H_2}}{W_{C_6H_6} Y_{H_2}}\right] e^{-\frac{4378}{T}} + c_3\left[\frac{\rho^2 Y_{C_2H_2} Y_{C_6H_6} Y_{C_6H_5} W_{H_2}}{W_{C_2H_2} W_{C_6H_6} W_{C_6H_5} Y_{H_2}}\right] e^{-\frac{6390}{T}}\right\} \quad (10)$$

$$\dot{\omega}_{M,inc} = \frac{M_p}{N_A}\dot{\omega}_{N,inc} \quad (11)$$

where c_2 and c_3 are the scaling factors, given as $c_2 = 127\times10^{8.88}, c_3 = 178\times10^{9.50}$, M_p $(=12011\,kg/kmol)$ is molar mass of a soot nucleus and N_A represents the Avogadro's number.

The second term in Eq.(5) represents the soot coagulation rate which is determined by Lindstedt [19] from the collision frequency (Puri et al.[20]).

$$\dot{\omega}_{N,coa} = -\left(\frac{24R}{\rho_{soot} N_A}\right)^{1/2}\left(\frac{6}{\pi\rho_{soot}}\right)^{1/6} T^{1/2} M^{1/6} N^{11/6} \quad (12)$$

The second term in Eq.(6) represents the surface growth of soot which is proposed by Frenklach et al. [21].

$$\dot{\omega}_{M,gro} = c_4\left(\rho\frac{Y_{C_2H_2}}{W_{C_2H_2}}\right) e^{-\frac{12100}{T}}\left[(\pi N)^{1/3}\left(\frac{6M}{\rho_{soot}}\right)^{2/3}\right] \quad (13)$$

where c_4 is a scaling factor, given as c_4=9000.6 kg.m.kmol^{-1}.s^{-1}, ρ_{soot} density of a soot particle, R the universal gas constant and W_i molecular weight of species, i.

The last term in Eq.(6) is the soot oxidation rate which is assumed to proceed through two reaction steps,

$$\frac{1}{2}O_2 + C_s \rightarrow CO \quad (14)$$

$$C_s + OH \rightarrow CO + H \quad (15)$$

Lee et al. [22] measured and modelled the O_2 and OH dependence of the soot oxidation in a laminar diffusion flame. By assuming that the kinetics of surface reactions are the limiting mechanism, the specific rate of soot oxidation is expressed by,

$$\dot{\omega}_{M,oxi} = -c_5\tau\rho\frac{Y_{OH}}{W_{OH}} T^{1/2}(\pi N)^{1/3}\left(\frac{6M}{\rho_{soot}}\right)^{2/3} - c_6\rho\frac{Y_{O_2}}{W_{O_2}} T^{1/2}(\pi N)^{1/3}\left(\frac{6M}{\rho_{soot}}\right)^{2/3} e^{-\frac{19778}{T}} \quad (16)$$

where $c_5 = 105.81 kg.m.kmol^{-1}.K^{-1/2}.s^{-1}$, $c_6 = 18903.51 kg.m.kmol^{-1}.K^{-1/2}.s^{-1}$ and a value of 0.13 is assigned to the collision efficiency, τ.

2.4. Numerical technique

Low speed solvers used in FDS [15] explicitly eliminate compressibility effects that give rise to acoustic (sound) waves for low-Mach number flows. The Boussinesq approximation invoked – the fluid is still considered thermally-expandable through the divergence of the flow. The temperature is extracted from the density via the equation of state. The fidelity of the numerical solution of the entire system of equations is tied to the pressure/velocity coupling thanks to a direct Poisson solver [15]. All spatial derivatives are approximated by second-order finite differences and the flow variables are updated in time using an explicit second-order predictor-corrector scheme. The convective terms are written as upwind-biased differences in the predictor step and downwind-biased differences in the corrector step. The thermal and material diffusion terms are pure central differences in both the predictor and corrector steps [15]. In this study, the fuel temperature of 300 K and the atmospheric pressure (P=1 atm) are imposed at the porous burner boundaries, conforming to the experimental conditions [5, 6]. At the free boundaries, zero gradient conditions are used for the farfield boundary values of the mass fractions.

3. Results and discussions

The sketch of the experimental setup [5, 6] with the relevant burner dimensions is displayed in figure 2(a, b). In the experiment, microgravity conditions are attained by means of parabolic flights that provide a gravity level of 10^{-3}g during 22 seconds. The experimental set-up corresponds to a square porous burner (L_p=W_p=5 cm, cf. figure 2b) which is embedded in the plane at z=0, centred in the y direction and at 5 cm from the inlet of a large enclosed combustion chamber. Porous burners have been used regularly in an attempt to simplify experiments by avoiding the coupling between heat feedback from the flame and fuel supply so that longer experimentation time can be achieved. The pyrolysis products of a condensed fuel are simulated by injecting ethylene with a constant velocity, $V_{F,}$ through a porous burner. Due to the limited space and amount of feed gases available in parabolic flight facilities, only small fuel rate can be accommodated. The dimensions of the computational domain, as shown in figure 2(a,b), are 8Lp in the windward direction, and 4Lp in both the lateral and normal directions so that boundary conditions can be set to conform as much as possible to the experimental configuration. The grid system contains 240 x 80 x 60 cells, and cells of 1 mm are concentrated around the reacting zone, giving the best trade-off between accuracy and cost for a three-dimensional reacting flow simulation. The resolution tests indicated that the computations are grid independent when the cell dimensions are lower than 2 mm. A further reduction in the grid size results in a significant reduction in the time step (Δt <0.0005 s) for satisfying the CFL stability condition [15]. As the experiment, an uniform oxidizer flow at the inlet with a composition of 35% oxygen and 65% nitrogen flows parallel to the surface with a constant velocity, V_{ox}=0.2 m/s. For describing the effects of pyrolysis rate in boundary layer with blowing, a dimensionless volume coefficient, C_q=V_F/V_{ox}, defined by Schlichting [23], is currently employed. It appears that three-dimensional phenomena in flame structure in low-speed concurrent flow are very rich in content as a function of the C_q.

This type flame can be described by the ratio between buoyant force and inertia one. This ratio is defined as follows, $\xi = \frac{Gr_x}{Re_x^{5/2}}$, where Re_x is the Reynolds number and Gr_x the Grashof number [24]. The experimental work [24] showed that in normal gravity, vigorous ejection of pyrolyzed fuel in the pyrolysis zone forms a vertical plume (cf. figure 3a) in the quiescent environment, indicating a predominant natural convection ($\xi > 1$). While microgravity reduces buoyancy enough to enable a much lower ratio ($\xi \le 1$) even for a low Reynolds number flow (Re<100). This induces a boundary layer diffusion flame (cf. figure 3b, c) with a significant change in the flame orientation and streamlines. The appearance of the predicted flame (cf. figure 4) is qualitatively similar to that

described by experiment for laminar diffusion flame (cf. figure 3c). The base of the flame is not attached to the gas fuel supply surface but is stabilized at significant stand-off height downstream. The total flame includes a blue flame plus orange zone. The leading edge portion of the flame consists of a blue region which appears more diffuse than the trailing one. Downstream of this initial zone, the remainder of the flame is orange-red streaks appearance, indicating a presence of great amounts of soot, and par consequent, a significant contribution to the heat flux on the surface.

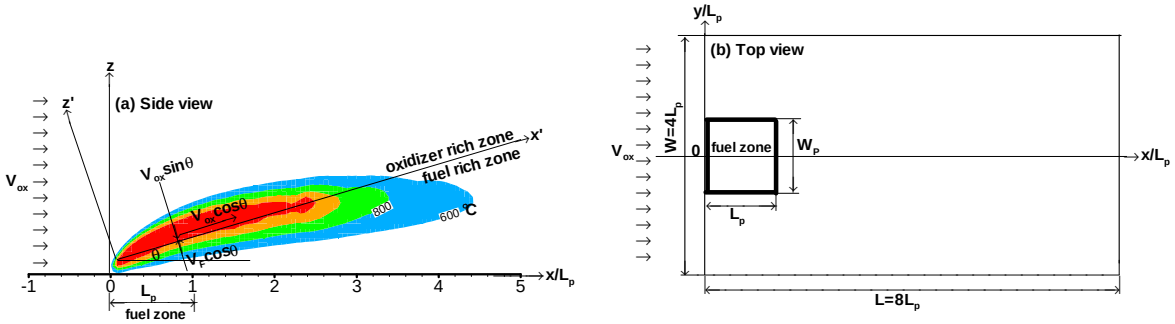

(a) Iso-contours of the temperature (side view) (b) Disposition of the fuel zone (top view)

Figure 2. Computational domain and the coordinate system

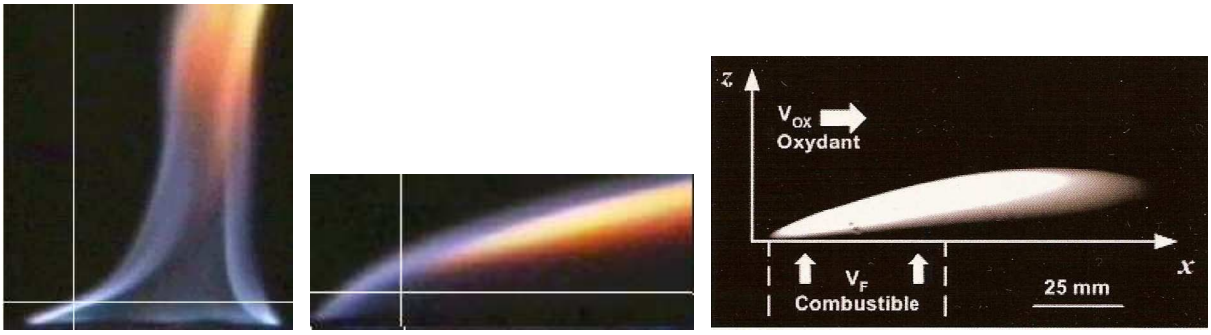

(a) Normal gravity (b) Micro-gravity (c) Micro-gravity

Figure 3. Structure of non premixed reacting flow from experiment

The predicted velocity field in vector form, is shown in figure 5. Energy release from an exothermic chemical reaction enhances the flow perturbations at the leading edge enough to enable a velocity overshoot along the line where fuel and oxidizer are delivered in stoichiometric proportions. The flow is controlled mainly by the cross-flow despite the surface blowing and the energy release due to combustion. The velocity profiles display a pronounced overshoot close to the flame zone at a low free stream velocity of 0.2 m/s. In normal gravity, the experimental work of Andreussi [25] indicated that a similar boundary layer velocity field is formed over a blowing surface only when the oxidizer stream velocity is larger than 1.2 m/s.

Reduced-gravity measurements are generally difficult to obtain, and so usually only the most easily measured quantities for a particular experimental configuration can be performed. This case is selected in this demonstration to clearly illustrate the peak temperature dependence on C_q at the trailing edge for the oxygen concentrations of 0.35. Both these measured and predicted values are presented in figure 6. The authors [5, 6] argued that thermocouples significantly perturb the flame in a low Reynolds number flow (Re<100), and thus, the measured flame temperature of 650°C clearly deviate from real flame temperature ranging from 1200-1600°C. In fact, an accurate determination of the flame temperature and heat flux could not be made due to the limited amount of microgravity time available. The prediction suggests that this characteristic temperature at the trailing edge is strongly dependent of C_q, and a temperature drop of approximately 450°C occurs with an increase of C_q from

0.02 to 0.08. The general characteristics of the flame temperature at the trailing edge include an initially gradual reduction in temperature level with C_q, followed by a rapid decrease in temperature until quenching. That means that rapid pyrolysis of the condensed fuel contributes to reducing the flame temperature below the adiabatic stoichiometric value.

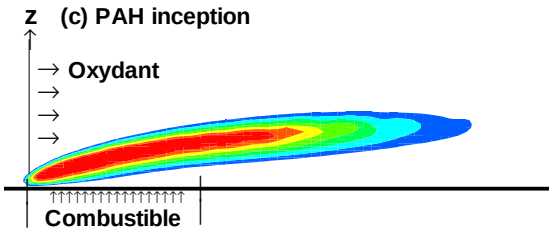

Figure 4. Predicted iso-contours of temperature

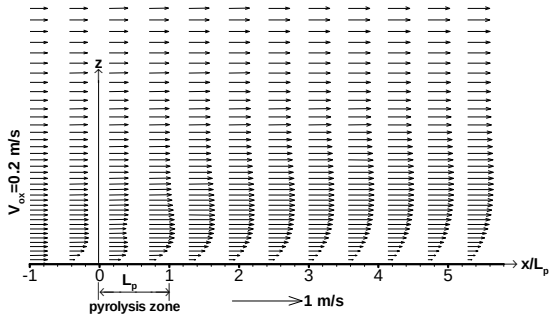

Figure 5. Predicted velocity vectors

The sooting behaviour of such laminar diffusion flame is characterized by using the laser induced incandescence technique (LII). The basic principle of LII relies on the detection of the thermal radiation from the soot particles that have been heated up to vaporization temperature by means of high energy laser pulse. Given in figures 7 and 8 is the comparison between the predicted and measured soot volume fractions across the height, z, at various axial locations x/L_p=0.5-1.75 for V_{ox}=0.25 m/s and V_F=0.005 m/s. By looking at their locations, the measured peak is placed just above the plate surface at z=3 mm, while the calculated one occurs at z=5 mm, with an over-prediction of the vertical stratification of the soot layer. A global description of the integrated soot production, F_{soot}, along x-axis as a function of V_F at an oxidizer velocity of 0.25 m/s is presented in figure 9. Soot volume fraction is integrated only over the soot layer in the z direction, as follows : $F_{soot}(x) = \int_{z=0}^{Z_{max}(x)} f_{soot}(x,z)dz$, where Z_{max} (x) is the height so that f_{soot} (x,z)=0 for $z>Z_{max}(x)$ at a given x. It seems that the PAH inception model reproduces the aforementioned sensitivity of the experimental soot formation to V_F. An enhancement of F_{soot} (cf. figure 9) from 20 to 38 (ppm)mm occurs with an increase of the fuel injection velocity, V_F, from 0.003 to 0.005 m/s. Thus, the shortest blue flame length and the longest yellow flame one (cf. figure 3b) are reached when the flame quenching occurs due to radiative loss with the highest fuel injection rate. The peak values of the integrated soot volume fraction are located far away from the trailing edge ($x/L_p>1$). It is found that the extent of the measured soot is always within the zone of $x/L_p<3$. It should be noted that the measured soot volume fraction distribution is converted from LII intensity image, and its accuracy depends on the accuracy of the proportionality constant required for correction due to attenuations of both the laser beam and the collected signal. Besides, for the low fuel injection velocity of V_F=0.003 m/s, the flames considered have the particularity of being mostly two-dimensional. While for high V_F, the flames considered develop strongly three-dimensional features far away from the trailing edge, affecting the collected signal for LII. This analyse is supported by the fact that the predicted soot profile follows closely the experimental trend for the low fuel injection velocity of 0.003 m/s, because the soot formation occurs within the extent of the collected signal for LII. While for the fuel injection velocity beyond 0.004 m/s, general shape of the predicted soot profiles has qualitative agreement with the experimental data. It is felt that the difference is due to a combination of experimental uncertainties and the error in the numerical simulation.

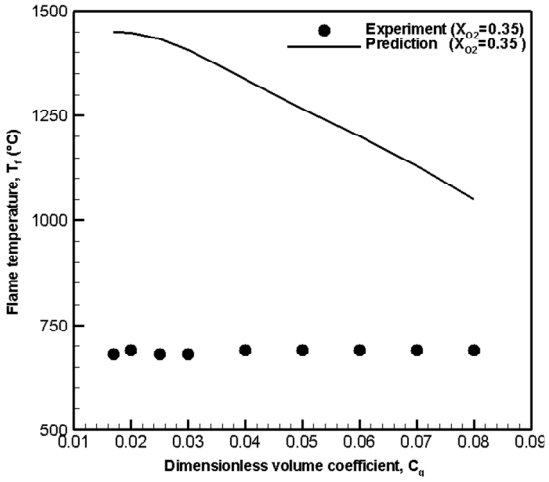

Figure 6. Effect of soot formation on the flame temperature as a function of C_q

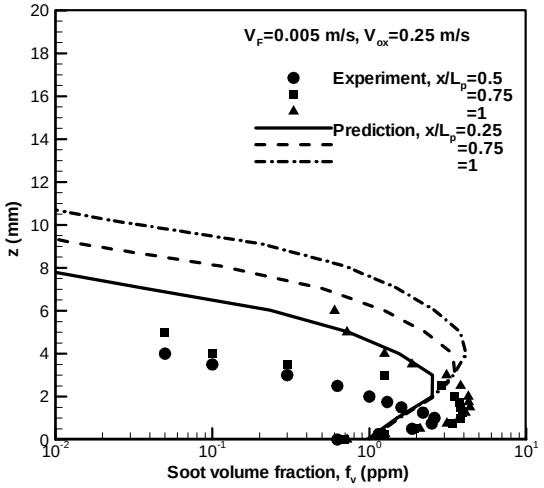

Figure 7. Comparison between computation and experiment for the soot volume fraction at the axial locations x/L_p=0.5-1

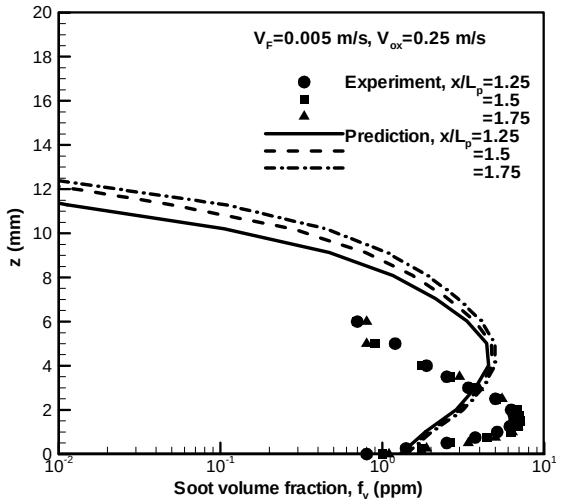

Figure 8. Comparison between computation and experiment for the soot volume fraction at the axial locations x/L_p=1.25-1.75

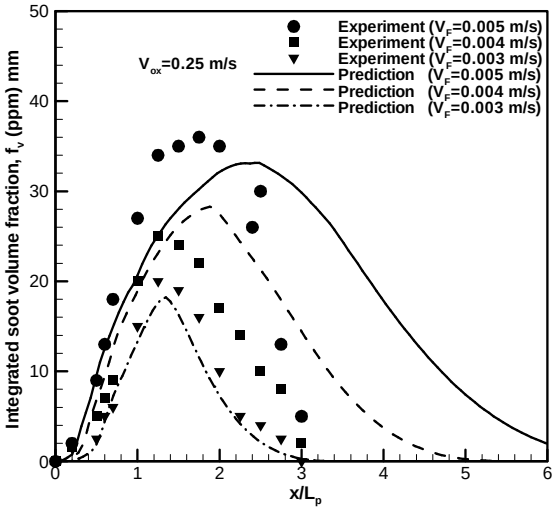

Figure 9. Comparison between computation and experiment for the integrated soot volume fraction at different fuel injection velocity

The trajectories of the jet diffusion flame and the velocity overshoots, characterized respectively by the flame stand-off distance d_T and the boundary layer thickness, d_V, in a cross-flow as a function of C_q are illustrated in figures 10 and 11. Because of radiative heat loss from this heavily sooting flame, the flame temperature does not surpass 1300ºC and decreases along the x-axis. The flame stand-off distance, d_T, is the distance of the 600°C contour from the plate (cf. figure 4), and this definition appears to be very close to the soot-radiating zone [5, 6]. The boundary layer thickness, d_V, is defined as the distance above the surface where the parallel component of velocity reaches 99% of the main flow velocity. In considering a wind-blown jet diffusion flame, it is convenient to identify various regions of flow within the jet flame. If the extent of each of these regions is considered to depend on C_q, then three flow regimes can be identified. In the first region, which extends from the fuel exit to the point where the wind forces first start to bend the jet diffusion flame, the momentum flux of the jet

flame itself is dominant and the physical characteristics of the jet flame are primarily a function of fuel injection velocity. The second transitional region extends from the end of the fuel injection velocity dominated regime to a point where wind effects begin to prevail. In the final region, the jet flame characteristics are dominated by the wind, with jet flame motion normal to the cross-wind being small. The diffusion flame stand-off distance, d_T, is an order of magnitude larger than that predicted by a Shvab-Zeldovich analysis, as described by Emmons [26] for a reacting boundary layer flow with blowing. The diffusion flame is shorter for the weak pyrolysis rate, and the isotherms are closer to the pyrolysis surface than those for the high one. Since the oxygen-side diffusion is the limiting factor in low-speed diffusive flames, an increase of C_q extends the reaction contour in the downstream direction and pushes the reaction zone far away from the plate surface due to the stoichiometric requirement. The flame stand-off and the boundary layer approach an asymptotical line once the C_q surpasses a critical value of 0.16, and reach a plateau as the flame quenching starts.

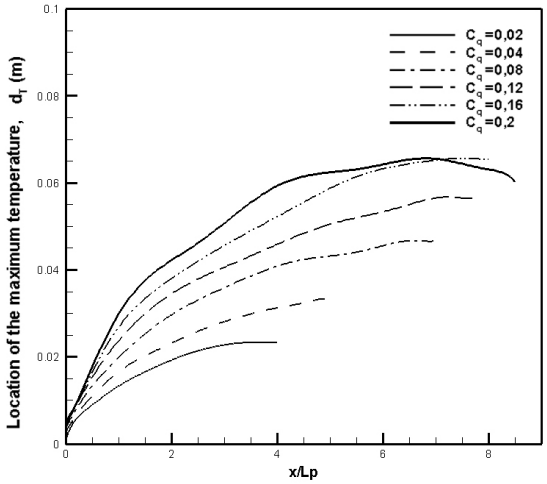

Figure 10. Evolution of the flame standoff distance for different C_q

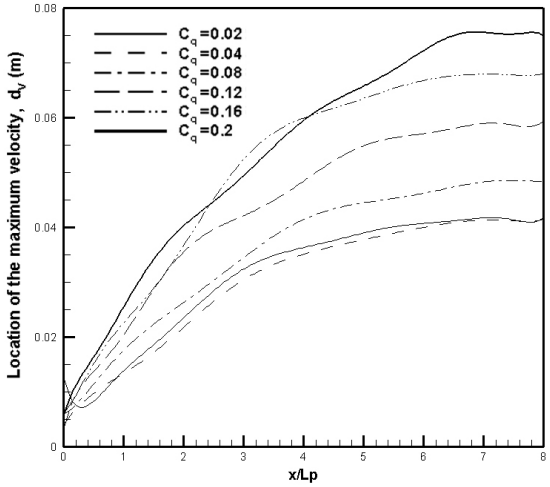

Figure 11. Evolution of the boundary layer thickness for different C_q

Given in figure 12 is the ratio, d_T/d_V, between the flame standoff distance, d_T, and the boundary layer thickness, d_V. Near the leading edge, the flame is positioned very close to the porous plate edge, and the flame establishes inside the viscous boundary layer ($d_T/d_V<1$), denoting the importance of oxygen-side diffusion which strengthens the flame. While soot formation shortens and weakens the blue flame near the leading edge through gas radiation loss with C_q. As x increases, both d_T and d_V move away from the plate into an area of higher velocity, and the ratio, d_T/d_V, converges to one single curve and toward a constant value of approximately 1.2, implying that the flame lies entirely outside the velocity boundary layer. The length of the soot-radiating zone attains a peak until blowoff. Once the flame quenching occurs, since most of the fuel remains in the core and is not participating in the combustion process, the trajectory of the maximum temperature is lower than the velocity one. An asymptotical solution established in natural convection from the reactive boundary layer model [26] suggests that the flame resides always within the boundary layer.

Figure 13 illustrates the ratio, d_H/d_T, between the trajectory of heat generation due to combustion and the flame standoff distance. The trajectory of heat release corresponds to an infinitely thin zone where fuel and oxidizer are delivered in stoichiometric proportions. In agreement with the findings of experiment [5, 6], the maximum temperature achieves on the side of the highly reacting fuel rich region ($d_H/d_T>1$) due to radiation loss. With an increase of C_q, the highest temperatures within the flame are found to approach the reacting zone ($d_H/d_T \approx 1$) due to blowing and thermal expansion. Thus under a zero gravity, the fluid and combustion are strongly coupled through the contributions of the

heat release and the thermal radiation associated with soot formation, inducing a major influence on the trajectory of the diffusion flame.

The trajectory of soot particles is obtained from the loci of the profile maxima of soot concentration. Contrary to the flame standoff distance, the maximum soot formation occurs always inside the boundary layer ($d_S/d_V<1$) far away from the stoichiometric line, as shown in figure 14. Soot particles trajectories inside a laminar boundary layer diffusion flame in microgravity do not follow exactly the gas movement due to thermophoretical effects, consistent with the observation of Fujita et al. [27]. This is evidenced by a significant deviation of soot particles from the stoichiometric line due to the dominant thermal expansion which prevents soot particles approaching the flame. The peak soot production is placed just over the plate surface in the fuel rich zone (cf. figures 7 and 8) for the small value of C_q=0.02. The trajectory where soot is delivered in abundance follows the response of flame standoff to changes in the main parameter of C_q.

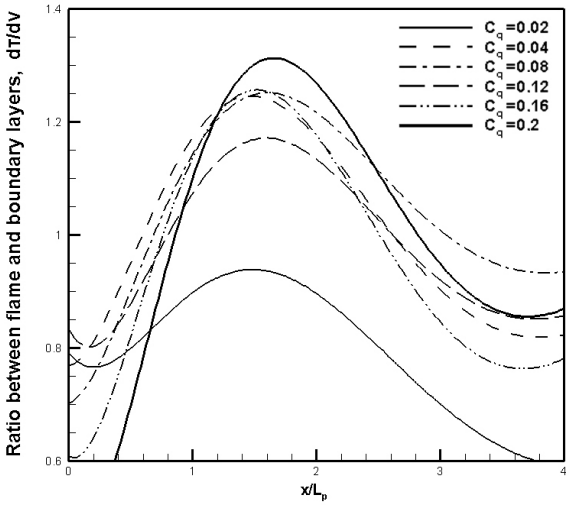

Figure 12. Ratio between flame standoff distance and boundary layer thickness for different C_q

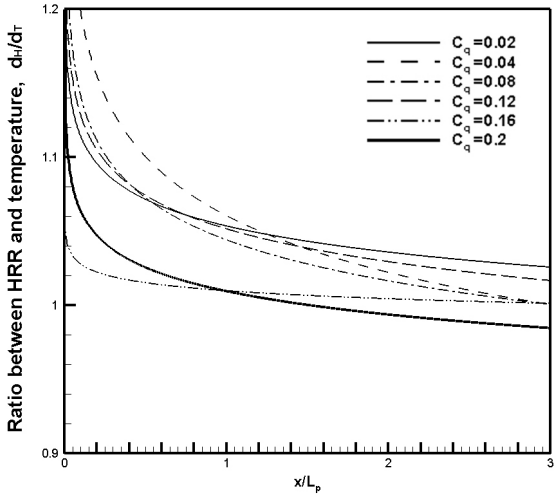

Figure 13. Ratio between the heat release trajectory and flame standoff distance for different C_q

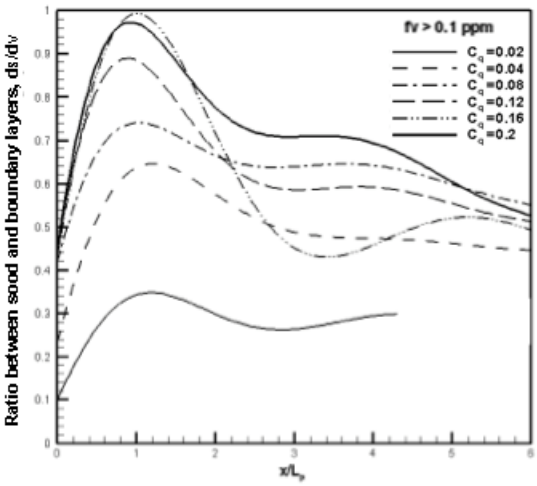

Figure 14. Ratio between soot and boundary layer thicknesses for different C_q

Contours of mean gas temperature on the symmetry plane are shown in figure15. A stable symmetrical flame and counter-rotating vortex in the cross-section are generated under microgravity conditions even with small value of C_q=0.02. The extent of the flame in cross-stream plane surpasses significantly the pyrolysis zone. Development of the counter-rotating vortex leads to the formation of the kidney-shape structure on the cross-stream plane for the temperature. This allows soot particle for long residence times before crossing the flame sheet at fuel-rich conditions, and enhances soot formation. This kidney shaped cross-section can be also characterized by the distance between the peak temperatures S_T, as shown in figure 16. Near the leading edge, the action of the counter-rotating vortices has not led to significant distortion of the temperature field with the contours appearing as its original single-flame. As downstream distance increases (x/L_p>2), the thermal expansion due to an exothermic chemical reaction enhances the air entrainment enough to enable the formation of the double-vortex motions. The action of these vortices is sufficiently strong to lead to two isolated regions with a peak temperature that are remote from the symmetry plane of the flame. The cross-stream contours of figure 15 shows that the main feature of the temperature field of the flame is again its kidney shaped cross-section, caused by the double-vortex motions. The distance S_T extends from the symmetry plane across the flame cross-section, but gradually migrated to the centre-line of the flame as downstream distance increases. Moreover, transition from its original single-flame to the kidney shape dual flame occurs earlier at low C_q due to the higher temperature level. Thus this is attributed to the competing effects between the flame temperature and the soot formation with C_q on the oxygen-side diffusion into the 3D flame.

In concurrent fire growth for a thick solid in microgravity condition, the fire growth rate correlates well with the flame heat feedback in the preheat zone. In microgravity, heat transferred by radiation ahead of a spreading flame is responsible for causing the flame to propagate. After a threshold pyrolysis temperature is attained, all heat flux to the material surface is used entirely for pyrolysis. The radiation heat flux in the preheat zone depends mainly on three factors: 1) the flame volume and its temperature level; 2) the concentrations of gaseous and particulate soot emitting species; 3) the view factor of the flame to the exposed material surface.

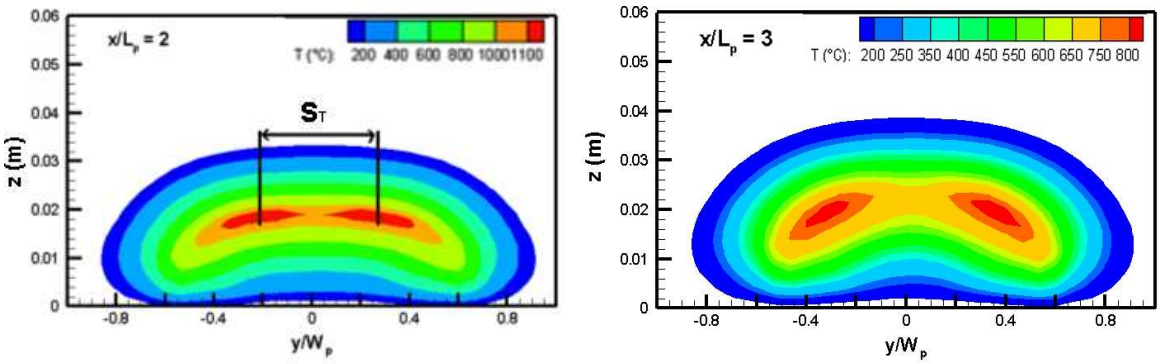

Figure 15. Cross-stream contours of the temperature at the axial locations x/L_p=2 and x/L_p=3

Given in figure 17 is the normalized total heat flux over a plate surface, where q_{pyro} is the heat release rate per unit area (kW/m^2) from a pyrolysis zone. Flame structure is of great importance on the heat flux over a material surface. The peak of the heat flux profile defines the location where the flame approaches to surface most closely. Microgravity flames are typically smooth (cf. figure 3b) with a large heat feedback just downstream the leading edge. The peak in the fraction of the total energy released by the flame to the surface increases from 5% to 15% with a rise of C_q due to increase in the flame volume. As downstream distance increases, the flame standoff distance becomes significant (cf. figure 10). Consequently, the maximum temperature moves away from the surface, implying a

reduction in the view factor from flame to the material surface. This leads to a decrease of the fraction of the total energy to the surface, approaching a value of about 3% in spite of C_q.

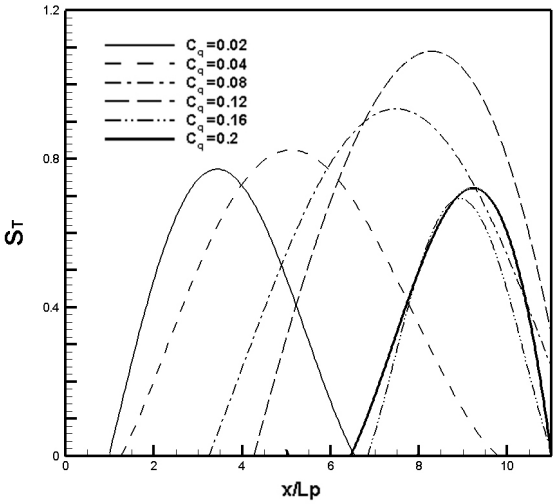

Figure 16. Evolution of the distance between the highest temperature position at a cross-stream section for different C_q

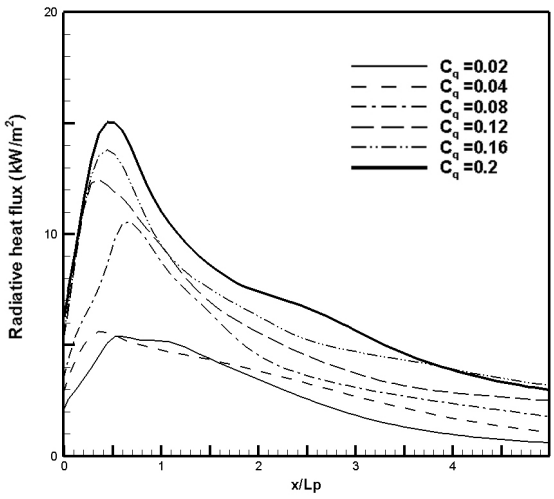

Figure 17. Normalized total heat flux over the horizontal surface for different C_q

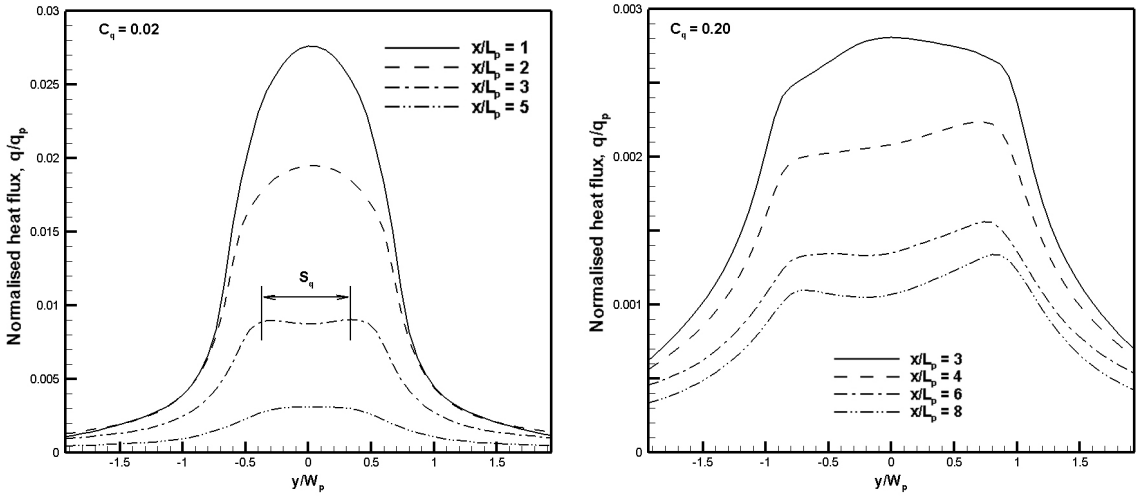

(a) C_q=0.02 (b) C_q=0.2

Figure 18. Evolution of the width of the high heat flux at different cross-stream sections

Turning finally to the thermal radiation profiles in a cross-stream section at different downwind stations, as shown in figure 18(a, b). The peak in the heat flux profile is consistent with the proximity of the flame to the surface. Gas temperatures are higher near the leading edge ($x/L_p<1$) of the flame, but the higher heat flux distribution is narrower for the small value of C_q. Downwind of the peak, the received heat flux falls off rapidly beyond the flame tip. The width scale S_q (cf. figure 18a) of the higher radiation flux as a function of C_q is illustrated in figure 19. The width S_q of the high heat flux increases noticeably when the flame becomes most obviously dual (cf. figure 15). Increase in C_q from 0.02 to 0.2 widens the soot-radiating orange zone, and consequently, the width of the higher radiation

flux increases almost four fold. However, the peak in the heat flux remains almost the same, independent of C_q. Obviously, the lower flame temperature and the increased soot formation with a rise of C_q are the competing effects to determine the magnitude of the flame heat feedback to the exposed material surface.

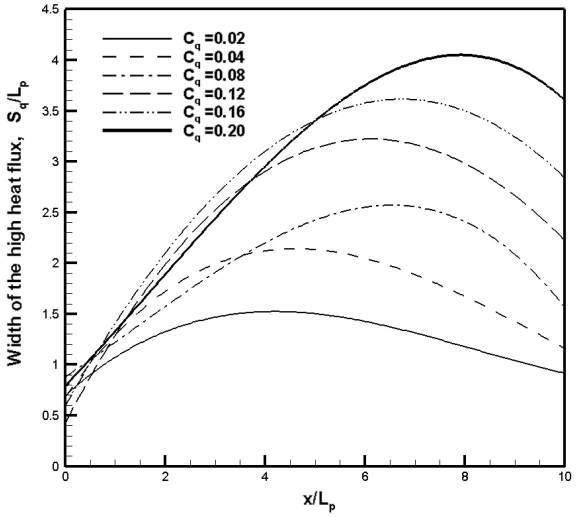

Figure 19. Ratio between the width of the high heat flux and the pyrolysis length for different C_q

4. Conclusions

This numerical study highlights the importance of soot formation on the structure of a microgravity diffusion flame established in a shear boundary layer. The behaviour of the soot production is reasonably well predicted by using PAH inception model. Both the prediction and the experiment suggest that soot production is enhanced with increasing the pyrolysis rate, further emphasizing the role of radiation on the geometric characteristics of a co-current, boundary layer laminar flame. It can be concluded that a large dimensionless volume coefficient favours soot formation, which shortens the blue flame near the leading edge due to radiation loss and strengthens the soot-radiating, orange-red flame. For a low Reynolds number reacting flow in microgravity, the flame establishes outside the viscous boundary layer far away from the leading edge, while the soot resides within the boundary layer. This implies the less importance of oxygen-side diffusion as compared to expansion and convection. A maximum in the flame length for oxidizer velocities below those encountered in natural convection, represents a greater hazard for fire safety in spacecraft.

These results are valid only for gaseous fuel and oxidizer, and should not be directly extrapolated to condensed fuel burning. Ongoing work should be focused on a proper definition of the transport processes for an accurate modelling of the solid phase using a pyrolysis reaction.

5. References

[1] Olson S L and T'ien J S 2000 *Combustion and Flame* **121(3)** 439-452
[2] T'ien J S 1990 *Combustion and Flame* **80** 335-357
[3] Konsur B, Megaridis C M and Griffin D W 1999 *Combustion and Flame* **118 (4)** 509-520
[4] Markstein G H and De Ris J 1985 *20th Symposium (international) on Combustion (*Pittsburgh: *The Combustion Institute*) 1637-46
[5] Legros G, Joulain P, Vantelon J P, Fuentes A and Torero J L 2006 *Combustion Science and Technology* 178-189

[6] Fuentes A, Legros G, Claverie A, Joulain P, Vantelon J P and Torero J L 2007 *31th Symposium (international) on Combustion (*Pittsburgh: *The Combustion Institute*) 2685-92
[7] Rouvreau S, Torero J L and Joulain P 2005 *Combustion Theory and Modelling* **9:2** 137-158
[8] Lui F, Guo H S, Gregory J, Smallwood J and Ömer L 2002 *J. of Quantitative Spectroscopy & Radiative Transfer* **73** 409-421
[9] Leung K M, Lindstedt R P and Jones W P 1991 *Combustion and Flame* 289-305
[10] Wen Z, Yun S, Thomson M J and Lightstone M F 2003 *Combustion and Flame* **135** 323-340
[11] Vovelle C, Delfan J L and Reuillon M 1994 *Soot Formation in Combustion* Springer-Verlag, Berlin 50-71
[12] Anderson H, McEnally C S and Pfefferle L D 2000 *28th Symposium (international) on Combustion (*Pittsburgh: *The Combustion Institute*) 2577-85
[13] Hall R J, Smooke M D and Colket M D 1997 *in Physical and Chemical Aspects of Combustion: A Tribute to Irvine Glassman, F.L Dryer and R.F Sawyer* (Ed.) Gordon & Breach 189-201
[14] Dagaut P and Nicolle A 2005 *Combustion and Flame* **140** 161-171
[15] Mcgrattan K B, Glenn P F and Jason E F 2010 *Fire Dynamics Simulator*
[16] Poinsot T and Veynante D 2005 *Theoretical and Numerical Combustion* second ed. Edwards
[17] Lutz A E, Kee R J, Grcar J F and Rupley F M 1997 *OPPDIF: A fortran computer program for computing opposed-flow diffusion flames* Sandia National Laboratories-Technical Rep. SAND96-8243
[18] Grosshandler W 1993 *National Institute of Standards and Thchnology* Maryland USA
[19] Lindstedt P R 1994 *Soot formation in Combustion, Springer-Verlag* 417-420
[20] Puri R, Richardson T F and Santoro R J 1993 *Combustion and Flame* **92 (3)** 320-333
[21] Frenklach M, Clary D W, Gardier J and Stein S E 1984 *20th Symposium (international) on Combustion (*Pittsburgh: *The Combustion Institute*) 887-901
[22] Lee K B, Thring M W and Beer J M 1962 *Combustion and Flame* **6** 137-145
[23] Schlichting H 1979 *Boundary layer theory* Seventh Edition McGraw-Hill
[24] Torero J L, Bonneau L, Most J M and Joulain P 1994 *25th Symposium (international) on Combustion (*Pittsburgh: *The Combustion Institute*) 1701-09
[25] Andreussi P 1982 *Combustion and Flame* **45** 1-6
[26] Emmons H 1956 *The film combustion of liquid fuel* Angews Z. Math. Mech. **36** 60-71
[27] Fujita O, Ito K, Ito H and Takeshita Y 1997 *4th NASA International Microgravity Combustion Workshop* 217-222